Current Management in a Hybrid Fuel Cell Power System: A Model Predictive Control Approach*

Ardalan Vahidi [†]   Anna Stefanopoulou   Huei Peng
Department of Mechanical Engineering, University of Michigan

Abstract

The problem of oxygen starvation in fuel cells coupled with air compressor saturation limits is addressed in this paper. We propose using a hybrid configuration, in which a bank of ultracapacitors supplements the polymer electrolyte membrane fuel cell during fast current transients. Our objective is to avoid fuel cell oxygen starvation, prevent air compressor surge and choke, and simultaneously match an arbitrary level of current demand. We formulate the distribution of current demand between the fuel cell and the bank of ultracapacitors in a model predictive control framework which can handle multiple constraints of the hybrid system. Simulation results show that reactant deficit during sudden increase in stack current is reduced from 50% in stand-alone architecture to less than 1% in the hybrid configuration. In addition the explicit constraint handling capability of the current management scheme prevents compressor surge and choke and maintains the state-of-charge of the ultracapacitor within feasible bounds.

1 Introduction

Fuel cells are electrochemical devices that convert the chemical energy of a hydrogen fuel into electricity through a chemical reaction with oxygen. The byproducts of this chemical reaction are water and heat. When compressed pure hydrogen is available, the subsystem that supplies oxygen to the cathode is one of the key controlled components of a fuel cell stack and is the subject of this paper. It is known in the fuel cell community that low partial oxygen pressure in the cathode reduces the fuel cell voltage and the generated power, and it can reduce the life of the stack. Song et. al. [1] show rapid drop in voltage when hydrogen or oxygen starvation occurs in phosphoric acid fuel cells. In a patent filed by Ballard [2] data shows that the fuel cell voltage is reversed during oxygen

starvation. Moreover the temperature within the fuel cell may rapidly increase when oxygen concentration is too low. Therefore the oxygen should be replenished quickly as it is depleted in the cathode. In high-pressure fuel cells a compressor is used to provide the required air into the cathode. The control challenge is that oxygen is depleted instantaneously when current is drawn from the stack, while the air supply rate is limited by the supply manifold dynamics and compressor operational constraints [3].

Air compressors can consume up to 30% of the fuel cell power during rapid increase in the air flow. Centrifugal compressors of the type used with high-pressure fuel cells, are susceptible to surge and choke that limit the efficiency and performance of the compressor [4]. Choke occurs at high mass flows, during step-up in compressor motor command and surge occurs at low mass flows, normally during a sudden step-down in compressor motor command. Surge is specially critical as it causes undesirable flow oscillations and instability and it can even result in backflow through the compressor and the installation downstream of the compressor [5]. Therefore extra measures need to be taken during step-down in demand to prevent compressor surge and during step-up to prevent choke. It is shown in [6] that control efforts targeting the compressor have a great potential for improving system performance.

In [3], it is shown that a combination of feedback and feedforward control of the compressor input, can improve the transient oxygen response. However the drop in oxygen level could not be eliminated by merely relying on compressor control unless the intention to change the load levels is known in advance. To protect against reactant starvation, Sun and Kolmanovsky [7] propose using a "load governor" which controls the current drawn from the fuel cell. The load governor ensures that constraints on oxygen level are fulfilled at the cost of slower fuel cell response to current demand. Air compressor constraints have not been explicitly addressed in the existing literature on fuel cell power systems.

One way to avoid a) fuel cell oxygen starvation b) compressor saturation, and c) simultaneously match an arbitrary level of current demand, is to add a rechargeable auxiliary current source which can respond quickly to a change in current demand. Splitting the current demand with a battery or an ultracapacitor for example offers additional flexibility in managing the electric loads. The battery or ultracapacitor can be connected with a fuel cell through a DC/DC converter as shown in Fig. 1. Other configurations of the electric connection between a fuel cell and an auxiliary energy supply are discussed in [8]. In all cases the auxiliary power source buffers the peaks in demand and can be recharged by the fuel cell itself, when the demand is lower. In this work we use a bank of ultracapacitors as the auxiliary power source to the fuel cell. We design a current splitting scheme which minimizes oxygen starvation and ultracapacitor usage while it enforces bounds on ultracapacitor's state of charge and prevents compressor surge and choke. The capability to explicitly handle constraints of the system is the motivation for using a model predictive control (MPC) approach in this problem.

The requirements for the supervisory controller formulated here are therefore different from those of existing power management schemes for hybrid vehicles. Most supervisory power split methods aim to minimize fuel consumption and enforce constraints of state
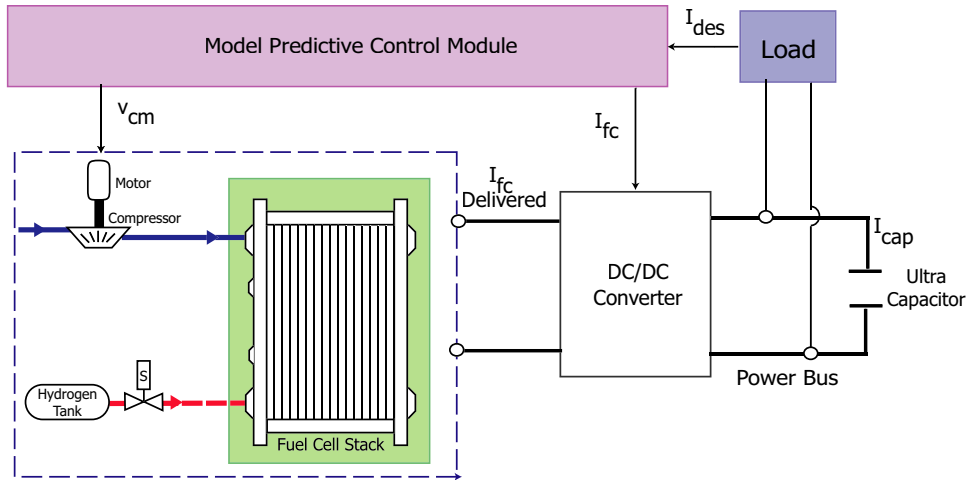
Figure 1: Schematic of the hybrid fuel cell control system. The fuel cell stack consists of 350 cells with peak power of 75 kW. The high pressure air supply is powered by a 12 kW compressor. A small auxiliary power source provides additional power when needed.

of charge of the auxiliary power source. Due to their emphasis in fuel consumption over a typical loading cycle the prior work can be categorized as: (i) "Rule-based" in which power splitting is based on instant demand [9, 10]. The advantage of these methods is their relative simplicity. However these methods cannot take into account simultaneous constraints in the interacting subsystems (ii) "Optimization-based" methods on the other hand, optimize the overall system performance over a decision horizon and can account for subsystem constraints. Dynamic programming (DP) is one of the optimization-based approaches that has been used for power management of hybrid electric vehicles. In most scenarios dynamic programming is used offline for a given load cycle and therefore is cycle specific [11, 12]. While most of these schemes are designed for hybrids with internal combustion engines, they can be applied to hybrids of fuel-cell with batteries or ultra-capacitors for vehicle [13, 14] or other applications [15]. Guezennec et al. [16] use a heuristic approach called "equivalent consumption minimization strategy" for power management of a fuel cell hybrid, which minimizes hydrogen consumption and regulates state of charge of the auxiliary power source. Rodatz et al. have used an optimal control design to minimize the hydrogen consumption in a hybrid fuel cell system [17]. Their design ensures that the auxiliary power source is charged at the end of each cycle.

The MPC controller that we formulate in this paper satisfies upper and lower bounds on the state of charge of the auxiliary power source and compressor constraints at all instances. Figure 1 shows the schematic of a fuel cell stack, the air compressor, a DC/DC convertor and the model predictive controller, which acts as the supervisory controller. The MPC unit determines the current drawn from the fuel cell (I_{fc}) and the compressor motor input (v_{cm}) to meet the control design specifications. In our model and problem formulation we assume that a lower level controller in the DC/DC convertor ensures that I_{fc} is drawn from the fuel cell [8], while the BUS voltage is regulated by the ultracapaci-

3

tor. This work is unique to our knowledge in that it takes into account compressor flow constraints in the supervisory control design stage. Inclusion of a more realistic ultracapacitor model and the compressor surge constraint in this paper are the major additions to our preliminary results presented in [18].

The next section describes the dynamic model of the fuel cell system followed by a description of the hybrid system architecture. Model predictive control formulation is briefly discussed in Sec. 4. In Sec. 5 we explain choice of prediction horizon and penalty weights, followed by nonlinear simulation results. Conclusions are given in Sec. 6.

2   Model of the Fuel Cell System

A nonlinear spatially-averaged model of a 75kW fuel cell stack together with its auxiliaries is developed in [19] based on electrochemical, thermodynamic and fluid flow principles. The fuel cell has 350 cells and can provide up to 300 A of current. The model, representing membrane hydration, anode and cathode flow and stack voltage, is augmented with the models of ancillary subsystems including the compressor, cooling system and the humidifier to obtain a nonlinear model of the overall fuel cell system. We assume that humidity and temperature are regulated to their desired levels and do not consider the effect of temperature or humidity fluctuations. This assumption should not limit the validity of our results since the temperature and humidity dynamics are considerably slower than the fuel cell power dynamics which we study in this paper. We have also assumed that a fast PI controller regulates the hydrogen flow to the anode to match the oxygen flow. Since the hydrogen is supplied from a compressed tank, a steady and timely hydrogen supply is assumed. The fuel cell model used in this work is identical to the one in [19, 20] and used in [3]. Note here that we do not use model simplifications used in [7, 21, 22]. Since the focus of this paper is on control of air flow, we present the governing equations, essential to understanding the dynamics between the compressor and the air flow into the cathode. The compressor flow, pressure, temperature and power characteristics are modelled using manufacturer maps [19, 20] and shown also in this section. For completeness, all the governing equations of this model are listed in the Appendix and consequently some equations appear twice; once in the main paper body and once in the Appendix.

To model the concentration of oxygen in the cathode, we first define a parameter called oxygen excess ratio λ_{O_2}:

$$\lambda_{O_2} = \frac{W_{O_2,in}}{W_{O_2,rct}}, \tag{1}$$

where $W_{O_2,in}$ is the flow of oxygen into the cathode and $W_{O_2,rct}$ is the mass of oxygen reacted in the cathode. Low values of λ_{O_2} indicate low oxygen concentration in the cathode or oxygen starvation. The rate of oxygen reacted $W_{O_2,rct}$, depends on the current drawn from the stack I_{fc}:

$$W_{O_2,rct} = M_{O_2} \frac{n I_{fc}}{4F}, \tag{2}$$

where n is the number of cells in the stack, F is the Faraday number, and M_{O_2} is the

4

oxygen molar mass. Therefore if the rate of air supply to the cathode is kept constant, λ_{O_2} decreases as more current is drawn from the stack. To maintain the level of oxygen excess ratio, more air should be supplied to the fuel cell. The flow rate of the oxygen into the stack $W_{O_2,in}$, is a function of the air flow out of the supply manifold W_{sm}:

$$W_{O_2,in} = y_{O_2} \frac{1}{1 + \Omega_{atm}} W_{sm}, \tag{3}$$

where $y_{O_2} = 0.21 \frac{M_{O_2}}{M_a^{atm}}$ is the mass ratio of oxygen in the dry atmospheric air and Ω_{atm} is the humidity ratio of the atmospheric air. The mass flow rate out of the supply manifold W_{sm}, depends on the downstream (cathode) pressure and upstream (supply manifold) pressure p_{sm}, through the orifice equation (A16). The total cathode pressure (A11) depends on the partial pressure of the (i) oxygen which is supplied $W_{O_2,in}$ (A18), oxygen which is reacted $W_{O_2,rct}$ (A26), and the oxygen removed $W_{O_2,out}$ (A23), (ii) nitrogen which is supplied (A19) and removed (A24) and (iii) the water which is supplied (A20), generated (A28), transported through the membrane (A29) and removed (A25). The additional cathode states of oxygen mass m_{O_2} (A1), nitrogen mass m_{N_2} (A2), water vapor mass $m_{w,ca}$ (A3), total return manifold pressure p_{rm} (A7), and anode states of hydrogen mass m_{H_2} (A8), and water vapor $m_{w,an}$ (A9), are needed to capture the temporal dynamics of the total cathode pressure during a step change in current. The derivation and physical interpretation of these equations are omitted here but can be found in [19]. However, to allow the reader understand how the control input affects the supply manifold flow W_{sm} and consequently the oxygen flow $W_{O_2,in}$, we add the following relations. Specifically the supply manifold pressure p_{sm}, and mass m_{sm}, are related to the compressor's air flow W_{cp}, and temperature T_{cp}, through the following dynamics:

$$\frac{dp_{sm}}{dt} = K_{sm}(W_{cp}T_{cp} - W_{sm}T_{sm}), \tag{4}$$

$$\frac{dm_{sm}}{dt} = W_{cp} - W_{sm}, \tag{5}$$

where K_{sm} is a coefficient determined by air specific heat coefficients and the supply manifold volume. The supply manifold temperature T_{sm} is defined by the ideal gas law (A14).

The compressor air flow W_{cp} and its temperature T_{cp} are determined using a nonlinear model for the compressor which has been developed in [19] for an Allied Signals centrifugal compressor that has been used in a fuel cell vehicle [23].

The compressor air mass flow rate W_{cp} is determined as a function of pressure ratio across the compressor and blade speed, using a compressor map shown in Figure 2. In this map, the dashed lines represent boundaries beyond which compressor surge and choke can occur. The equations used here to represent compressor dynamics are valid within these bounds. Later in this paper we enforce point-wise-in-time constraints to ensure operation of the compressor inside the bounded region and away from the surge and choke regions.
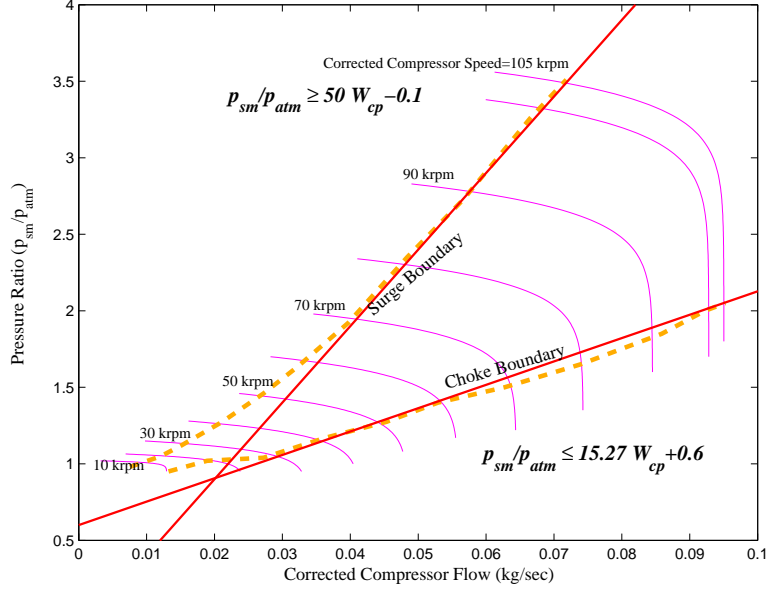
Figure 2: The compressor map

In our simulations this map is modelled using a nonlinear curve-fitting technique, which calculates compressor air flow as a function of inlet pressure p_{atm}, outlet pressures p_{sm} and compressor rotational speed ω_{cp}:

$$W_{cp} = f(\frac{p_{sm}}{p_{atm}}, \omega_{cp}) \tag{6}$$

The details of compressor flow calculation are shown in equation (A34)-(A43) in the Appendix. The compressor outlet temperature and the torque required to drive the compressor are calculated using standard thermodynamic equations [24, 25]. The temperature of the air leaving the compressor is calculated as follows:

$$T_{cp} = T_{atm} + \frac{T_{atm}}{\eta_{cp}} \left[\left(\frac{p_{sm}}{p_{atm}} \right)^{\frac{\gamma-1}{\gamma}} - 1 \right] \tag{7}$$

where $\gamma = 1.4$ is the ratio of the specific heats of air, η_{cp} is the compressor efficiency and T_{atm} is the atmospheric temperature. The compressor driving torque τ_{cp} is:

$$\tau_{cp} = \frac{C_p}{\omega_{cp}} \frac{T_{atm}}{\eta_{cp}} \left[\left(\frac{p_{sm}}{p_{atm}} \right)^{\frac{\gamma-1}{\gamma}} - 1 \right] W_{cp} \tag{8}$$

where C_p is the specific heat capacity of air. The compressor rotational speed ω_{cp} is determined as a function of compressor motor torque τ_{cm} and the torque required to drive the compressor τ_{cp}:

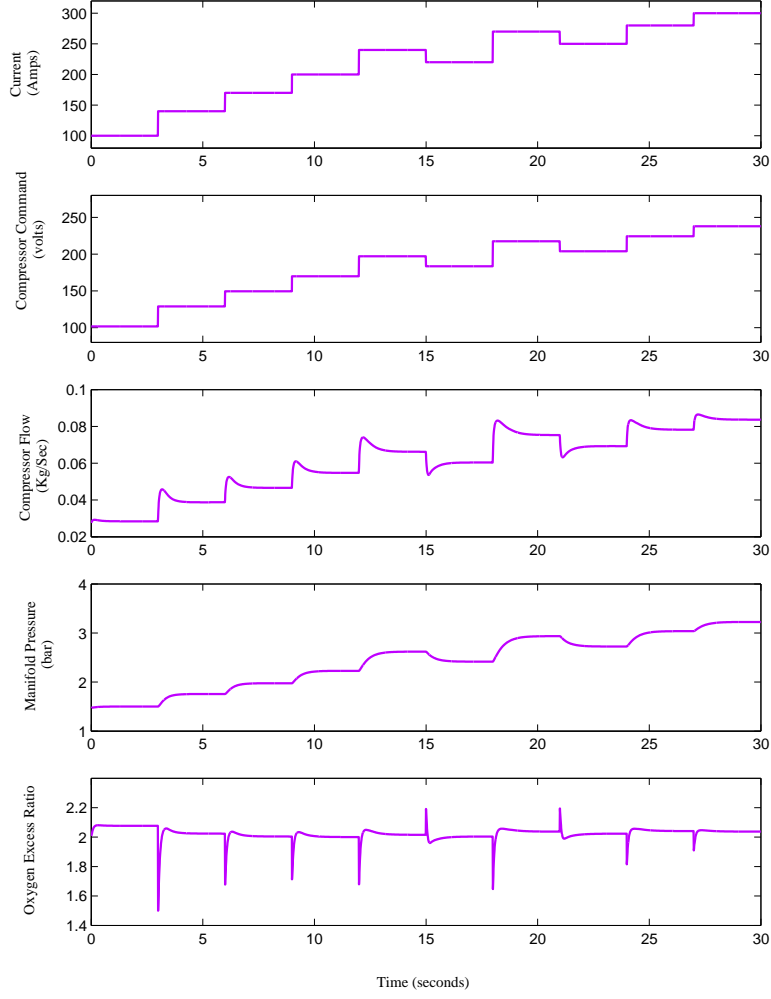$$J_{cp} \frac{d\omega_{cp}}{dt} = \tau_{cm} - \tau_{cp} \tag{9}$$

6

Figure 3: The fuel cell response to step changes in current demand.

where J_{cp} is the compressor inertia. The compressor motor torque τ_{cm} is calculated as a function of motor voltage v_{cm} using a DC motor model:

$$\tau_{cm} = \eta_{cm} \frac{k_t}{R_{cm}} (v_{cm} - k_v \omega_{cm}) \tag{10}$$

where k_t, R_{cm} and k_v are motor constant and η_{cm} is the motor mechanical efficiency.

In summary, the compressor voltage v_{cm}, controls the speed of the compressor through the first-order dynamics shown in (9) and (10). The speed of the compressor determines the compressor flow rate W_{cp}, which then according to equation (4), affects the supply manifold pressure p_{sm}. The latter, together with the cathode pressure, determines the supply manifold flow W_{sm}, and the flow rate of the oxygen into the cathode $W_{O_2,in}$ which finally affects the excess ratio λ_{O_2} given in equation (1).
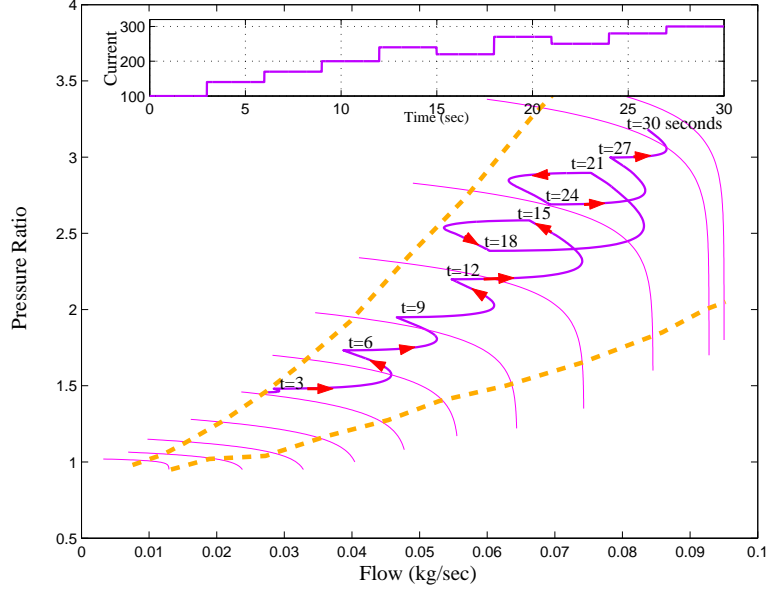
7

Figure 4: The compressor response to step changes in current demand.

The set of equations described above form the fuel cell state space equations:

$$\dot{x}_{fc} = h(x_{fc}, u)$$
$$u = [v_{cm} \quad I_{fc}]^T \tag{11}$$
$$y = [W_{cp} \quad p_{sm} \quad \lambda_{O_2}],$$

where $x_{fc} = [m_{O_2} \quad m_{H_2} \quad m_{N_2} \quad w_{cm} \quad p_{sm} \quad m_{sm} \quad m_{w,an} \quad p_{rm}]^T$ is the state vector of the nonlinear dynamic system from $u = [v_{cm} \quad I_{fc}]^T$ to the outputs compressor flow, manifold pressure and oxygen excess ratio.

Figure 3 shows the nonlinear simulation results for the model during a series of step changes in current. During the current steps, the compressor motor input is calculated as a function of current drawn from the fuel cell based on a feedforward map. This linear map is designed such that at steady-state the oxygen excess ratio is regulated at the value of 2. The figure shows current, compressor input, compressor flow, manifold pressure and oxygen excess ratio. It can be seen that while the compressor flow and manifold pressure increase when the current increases, an undesirable rapid drop in oxygen excess ratio still occurs during sudden changes in current levels.

Figure 4 shows the evolution of the flow and pressure ratio in the compressor map during these transients. During a step-up in v_{cm} command, the compressor flow increases faster than the pressure p_{sm} downstream the compressor. As a result the compressor operates near the choke boundary. During a step-down in v_{cm}, the operating trajectory nears the surge boundary. Larger steps in current require larger compressor commands that if applied instantaneously may result in surge or choke. Slowing down the compressor command through a filter could help prevent the surge or choke of the compressor but

8

will deteriorate regulation of oxygen in the cathode. An auxiliary power source added to the fuel cell provides more flexibility when dealing with these constraints. The next section explains the addition of the auxiliary power source to the fuel cell model.

3 The Hybrid Fuel Cell and Ultracapacitor Configuration

In absence of an auxiliary power source, the current drawn from the fuel cell acts as an external disturbance and its sudden increase results in oxygen starvation or compressor surge. By adding a fast power source, part of the power demand can be drawn from the auxiliary source, giving the fuel cell and the compressor time to adjust to the new power levels. To respond to rapid increase in demand, the auxiliary power source delivers power for short periods of time. This power requirement is best achieved by ultracapacitors which typically have a power density ten times higher than batteries [13]. Unlike batteries, ultracapacitors store energy in the form of electrical charge. The stored charge in an ultracapacitor is characterized by a normalized measure called the state of charge, $SOC \in [0, 1]$. We associate the state of charge of 0 and 1 to the minimum and maximum allowable charge respectively. The ultracapacitor operating voltage can be maintained within a band by appropriate sizing of the ultracapacitor and enforcing upper and lower bounds on state of charge.

The rate of change in ultracapacitor state of charge is proportional to the charging current, I_{cap} [26]:

$$\frac{d}{dt}SOC = \frac{1}{Cv_{max}}I_{cap} \tag{12}$$

where C is the capacitance of the ultracapacitor in Farads and v_{max} is its voltage at full charge. In our design we fix the maximum BUS and therefore ultracapacitor voltage to 350 volts. We choose the capacitance to be 0.65 Farads which is a sufficiently large power buffer during fuel cell load transients. One possible configuration that realizes this value of capacitance, is a bank of 120 ultracapacitors, each with capacitance of 80 Farads and a rated voltage of 3 volts, connected in series. Together the package of ultracapacitors can provide a maximum voltage of 360 volts and a storage capacity of 11 Watt-hours. This size of ultracapacitors can shield the fuel cell from starvation or prevent compressor surge. Note here that larger capacitances will be potentially needed for start-up or other power requirements.[1]

In the hybrid fuel cell-ultracapacitor system, we assume that the response time of the ultracapacitor is considerably faster than the response time of the fuel cell. This is a valid assumption, since the time constant of the small ultracapacitors used in this application is very small. If the current demand is feasible, that is, if the current demand

---

[1]In [13], Rodatz et al. have used ultracapacitors in a hybrid fuel cell vehicle to assist the fuel cell during hard accelerations and for storing the energy from regenerative braking. A much larger buffer size is required for their purpose. They have provided this buffer by 282 pair-wise connected capacitors, each with capacitance of 1600 F. The storage capacity is 360 Watt-hours.

does not exceed the capacity of the hybrid system, it can always be met by the fuel cell or combination of fuel cell and the ultracapacitor. The current delivered by the DC/DC convertor from the fuel cell is:

$$I_{dc} = \frac{\eta_{dc} I_{fc} v_{fc}}{v_{cap}} \tag{13}$$

where η_{dc} is the convertor efficiency which we fix at 0.95, I_{fc} and v_{fc} are the fuel cell stack current and voltage respectively. The stack voltage v_{fc} is a nonlinear function of partial pressure of oxygen in the cathode and hydrogen in the anode, stack temperature and fuel cell current. The detailed fuel cell voltage model can be found in [19]. The ultracapacitor voltage v_{cap}, is a linear function of its state of charge:

$$v_{cap}(t) = SOC(t) v_{max}. \tag{14}$$

As shown in Fig. (1),the requested current I_{des} can be met by the fuel cell and convertor as follows:

$$I_{des} = I_{dc} + I_{cap} \tag{15}$$

The current $I_{cap} = I_{des} - I_{dc}$ is provided by the ultracapacitor when positive. Negative I_{cap} means that the fuel cell is charging the ultracapacitor. The charging current would then be $I_{dc} - I_{des}$. Therefore Eq. (12) can be rewritten as follows:

$$\frac{d}{dt} SOC = \frac{1}{C v_{max}} \left(\frac{\eta_{dc} I_{fc} v_{fc}}{SOC v_{max}} - I_{des} \right) \tag{16}$$

This nonlinear equation is coupled with the nonlinear fuel cell equation (11) through the I_{fc} term.

For the control design purpose, the nonlinear model of the hybrid system consisting of (11) and (16) is linearized around a selected operating point. We define nominal stack current of $I_{fc}^0 = 190$ Amps. The nominal desired current is also selected at $I_{des}^0 = 190$. The nominal value for oxygen excess ratio is selected at $\lambda_{O_2}^0 = 2.0$, which corresponds to maximum fuel cell net power for the nominal current [20]. The compressor motor voltage needed, to supply the optimum air flow that corresponds to $I_{fc}^0 = 190$ and $\lambda_{O_2}^0 = 2.0$, is $v_{cm}^0 = 164$ volts. The state of charge of the ultracapacitor at this nominal operating point is $SOC^0 = 0.61$.

Equations (11) and (16) are linearized around the above operating points and then discretized to obtain the equations for the hybrid system:

$$x_{hb}(k+1) = A x_{hb}(k) + B_u u(k) + B_w w(k) \tag{17}$$

$$y_{hb}(k) = C x_{hb}(k) + D_u u(k) \tag{18}$$

where $x_{hb} = [\delta x_{fc} \quad \delta SOC]^T$ and the operator δ indicates deviation from the operating point. The control command is $u = [\delta v_{cm} \quad \delta I_{fc}]^T$ and the disturbance is the change in current demand $w = \delta I_{des}$, which is treated as a measured disturbance. The outputs are compressor flow, manifold pressure, oxygen excess ratio and state of charge, therefore:

$$y_{hb}(k) = [\delta W_{cp} \quad \delta p_{sm} \quad \delta \lambda_{O_2}(k) \quad \delta SOC(k)]^T.$$

The control objective is to find the control u that regulates oxygen excess ratio and state of charge of the ultracapacitor to desired setpoints. To avoid large variations in the BUS voltage, it is also required that state of charge of the ultracapacitor always remain within nominal bounds:

$$-0.05 \leq \delta SOC \leq 0.05 \tag{19}$$

As a result the BUS voltage is bounded between 200 and 230 volts. Moreover the controller should ensure that the compressor always operates away from surge and choke boundaries. As shown in Fig. (2) the boundaries that define the surge and choke regions can be approximated by a linear combination of compressor flow and compressor pressure ratio. The surge and choke constraints can then be represented by two linear inequalities:

$$\begin{aligned} -0.0506\delta W_{cp} + \delta p_{sm} &\leq 0.4, \\ 0.0155\delta W_{cp} - \delta p_{sm} &\leq 0.73. \end{aligned} \tag{20}$$

Both compressor flow and pressure ratio are functions of states of the system and are relatively easy to measure. Note here that by confining the compressor between the surge and choke boundaries, the region for which the nonlinear fuel cell and compressor models can be approximated by a linear model is increased. So the compressor constraints address both functional and procedural requirements. To better handle these constraints a model predictive control methodology is applied using the linearized fuel cell, electric compressor and ultracapacitor models.

4   Control Design

The constrained control problem described above can be solved using a model predictive controller [27]. In this paper we use a simple version of MPC called Dynamic Matrix Control (DMC). For a survey of other formulations applied in industry the reader can refer to [28]. A good review of conditions for stability and optimally of MPC is presented in [29]

Here we use the linear model of the hybrid system presented in equations (17) and (18) for prediction and control design and then apply the control to the nonlinear fuel cell-ultracapacitor model (11) and (16). First to remove the direct injection of control input u to the hybrid output equation (18), we filter the two inputs through linear first order filters with unity gain and very fast time constants. When the system equations (17) and (18) are augmented with the two filter states, the new augmented system is:

$$\begin{aligned} x_a(k+1) &= A_a x_a(k) + B_{a,u}u(k) + B_{a,w}w(k) \\ y(k) &= C_a x_a(k) \end{aligned} \tag{21}$$

in which

$$x_a = [x_{hb} \quad x_u]^T, \quad u = [\delta v_{cm}, \quad \delta I_{fc}]^T, \quad w = \delta I_{des}$$

and x_u are the two filter states.

To account for the difference between the nonlinear and the linear models, a simple step disturbance observer is used. In nonlinear simulations the actual plant output $y_p = [W_{cp} \quad p_{sm} \quad \lambda_{O_2}(k) \quad SOC(k)]^T$ is obtained using the nonlinear fuel cell model (11) coupled with the ultracapacitor charge dynamics (16). At each instant k the disturbance $\hat{d}(k|k)$, is estimated as the difference between the plant and the linear model outputs:

$$\hat{d}(k|k) = y_p(k) - C_a\hat{x}_a(k|k-1) - y^0 \tag{22}$$

where $\hat{x}_a(k|k-1)$ is the state of the linear model for instant k predicted at instant $k-1$, y_p is the plant output and y^0 represents the outputs at the operating point. It is assumed that future values of measured disturbance, $\hat{w}(k+j|k)$, and estimator error, $\hat{d}(k+j|k)$, remain constant during the next prediction horizon:

$$\begin{aligned} \hat{w}(k+j|k) &= w(k) \\ \hat{d}(k+j|k) &= \hat{d}(k|k). \end{aligned} \tag{23}$$

Now the linear model can be used to estimate the states and the outputs using the following observer with observer gains L_x and L_y [27]:

$$\begin{aligned} \hat{x}_a(k+j+1|k) &= A_a\hat{x}_a(k+j|k) + B_{a,u}u(k+j) + B_{a,w}\hat{w}(k+j|k) + L_x\hat{d}(k+j|k) \\ \hat{y}(k+j|k) &= C_a\hat{x}_a(k+j|k) + L_y\hat{d}(k+j|k) \end{aligned}$$
$$\tag{24}$$

where $\hat{x}_a(k+j|k)$ and $\hat{y}(k+j|k)$ are the estimate of the state and output at instant $k+j$ based on information available at instant k. We choose L_y to be a unit vector, which implies that after each measurement the model outputs are replaced by the actual plant outputs. This ensures that the output predictions are updated by actual outputs of the plant at each step. The gain L_x is chosen to place the state estimator poles inside the unit circle. Interested reader can find more details about other possible disturbance models in [30, 31].

The control inputs $u(k+j)$ are the unknowns that are calculated at each step. If the control horizon is N and prediction horizon is P, a control sequence

$$u^N = [u(k) \quad u(k+1) \quad ... \quad u(k+N-1)]^T$$

is sought at each instant k, which minimizes the following finite horizon performance index:

$$J = \sum_{j=1}^{P} \left(\|(r(k+j) - \hat{y}(k+j|k))\|_Q^2 + \|\Delta u(k+j-1)\|_S^2 \right) \tag{25}$$

and satisfies the surge, choke and state-of-charge constraints for all k. The constraints given by (19) and (20) can be described as a function of predicted outputs as follows:

$$\begin{bmatrix} -0.0506 & 1 & 0 & 0 \\ 0.0155 & -1 & 0 & 0 \\ 0 & 0 & 0 & 1 \\ 0 & 0 & 0 & -1 \end{bmatrix} \hat{y}(k+j|k) \leq \begin{bmatrix} 0.4 \\ 0.73 \\ 0.05 \\ 0.05 \end{bmatrix}, \quad j = 1, 2, \ldots, p \tag{26}$$

In the performance index, S and Q are input and output weighting matrices respectively. Specifically $Q = diag(Q_{W_{cp}}, Q_{p_{sm}}, Q_{OER}, Q_{SC})$ and $S = diag(S_{cp}, S_I)$, where $Q_{W_{cp}}$, $Q_{p_{sm}}$, Q_{OER} and Q_{SC} are penalties on compressor flow, manifold pressure, oxygen excess ratio and state of charge respectively. S_{cp} and S_I are penalties on compressor motor input and current drawn from the fuel cell. We chose $Q_{W_{cp}} = 0$, $Q_{p_{sm}} = 0$ so that the the first two outputs are not penalized in the performance index and are only used for checking the constraints. At each sampling instant k, the plant output $y_p(k)$, and the disturbance $w(k)$, are measured. The estimation error $\hat{d}(k|k)$ is calculated using equation (22). The reference $r(k+j)$ is also fixed. Based on the assumption that future values of measured disturbances remain constant during the next prediction horizon, $\hat{y}(k + j|k)$ can be calculated as a function of the control sequence u^N, only. The performance index (25) and the constraints (26) can be written as functions of u^N, output and disturbance measurements, and the reference command in a quadratic form. Quadratic programming is used to solve this constrained optimization problem at each sampling time. In absence of constraints, the problem reduces to a simple minimization problem and an explicit control law can be calculated. With constraints, on the other hand, a straightforward explicit control law does not exist. Instead numerical optimization of the performance index is carried out online to find the control input [2].

5   The Simulation Results and Discussion

We first tune the prediction horizon and the penalty weights using the linearized model of the plant. The control design is then verified with the actual nonlinear model of the plant. The desired values for regulated outputs is fixed for all times at $\lambda_{O_2}^{des} = 2$ and $SOC^{des} = 0.61$. We used a sampling frequency of 50 Hz. In this paper the control horizon is chosen equal to the prediction horizon. The length of prediction horizon is influential in both the computational time and performance of the system. Figure 5 shows the influence of choice of prediction horizon on performance in linear unconstrained simulations. The location of the dominant pole is shown in the s-domain through $z = e^{s\Delta T}$ transformation [33] as prediction horizon is increased from two to fifty sampling steps. It is clearly shown that, a short prediction horizon results in a pair of unstable closed loop poles. If the state of charge is not heavily penalized and if the prediction horizon is short, the controller will use the ultracapacitor aggressively to regulate the air flow in this short horizon. The "short-sighted" and aggressive use of the ultracapacitor can result in an unstable closed-loop system. Based on this analysis we chose 40 sampling steps for the prediction horizon to avoid poor performance and prevent instability.[3]

---

[2]It can be shown that with linear constraints, the control is a piecewise linear function of the states. However analytical calculation of such a function becomes increasingly difficult as larger prediction horizons are used [32].

[3]In recent formulations of MPC, an infinite horizon cost function is used and transformed into a cost function with finite horizon and a terminal penalty to guarantee nominal stability [34]. In practice increasing the length of the prediction horizon is a common way to enhance the nominal stability [35].
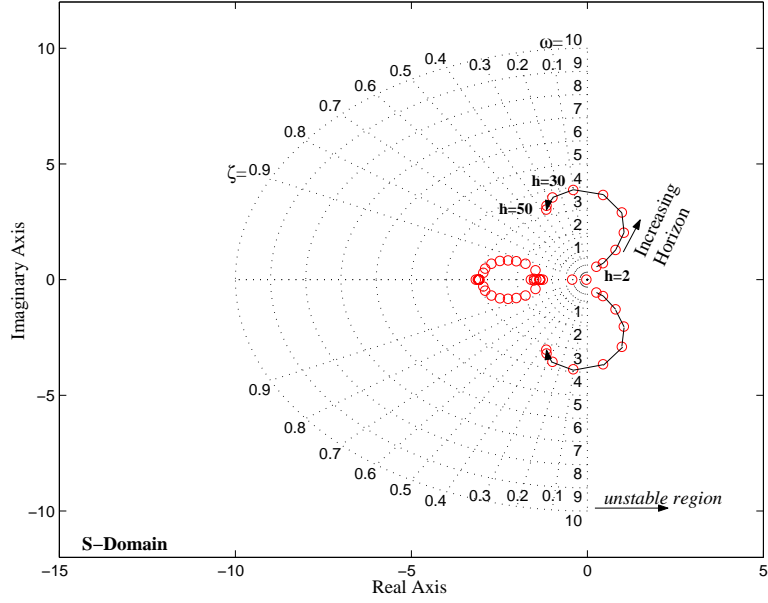
Figure 5: Loci of closed-loop poles in s-domain as prediction horizon increases from h=2 to h=50 steps. The performance index weights are $Q = diag(0, 0, 100, 1)$, $S = diag(0.1, 0.001)$
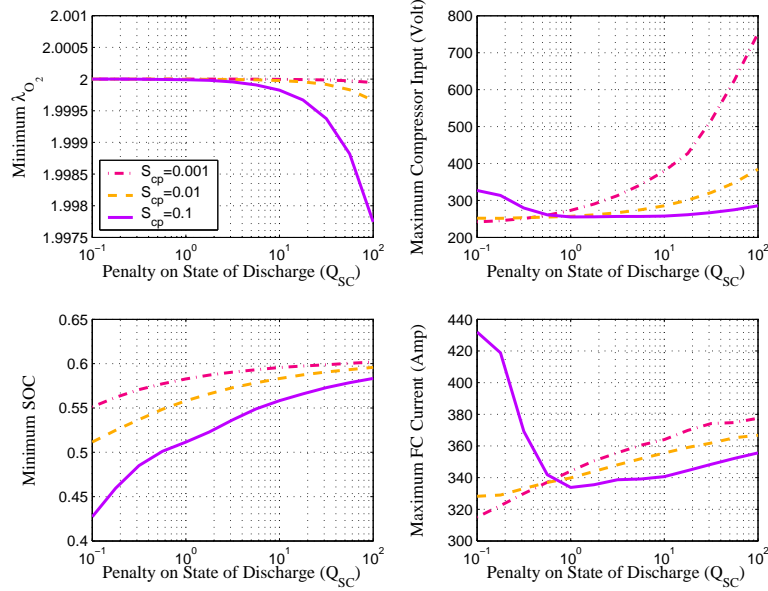

Figure 6: Worst input and output values for different selection of penalty on compressor input, S_{cp}, and penalty on SOC, Q_{SC}, when demand jumps from 191 to 291 Amps. Penalty on oxygen is fixed at $Q_{OER} = 100$ and penalty on current is fixed at $S_I = 0.001$.
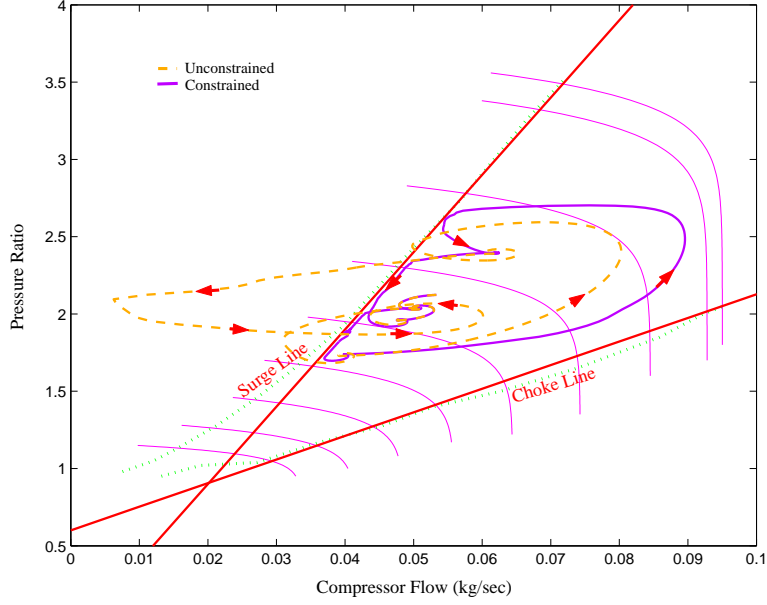
14

Figure 7: Compressor flow trajectory with and without surge constraint. The performance index weights are $Q = diag(0, 0, 100, 1)$, $S = diag(0.1, 0.001)$.

The effect of penalty weights on the controller performance is studied next. Consider $Q = diag(0, 0, Q_{OER}, Q_{SC})$ and $S = diag(S_{cp}, S_I)$ in the performance index (25). The weight on the state of charge, Q_{SC} determines the extent to which the ultracapacitor is used. Figure 6 shows the influence of the weights on maximum deviation from nominal values of inputs and outputs as the current demand increases from 191 to 291 Amps[4]. In each plot, the x-axis shows the penalty on the state of charge and each curve corresponds to a different penalty on compressor voltage. Penalty on OER is fixed at 100 and penalty on current is fixed at $S_I = 0.001$. Based on Fig. 6, we chose the penalty on state of charge to be 1 and the penalty on compressor input at 0.1. These values result in good oxygen regulation with minimum compressor use and maximum utilization of the ultracapacitor (minimum SOC almost equal to 0.5) for 100 Amps increase in current. Therefore for the rest of simulations, the penalty matrices $Q = diag(0, 0, 100, 1)$ and $S = diag(0.1, 0.001)$ are fixed.

After a suitable prediction horizon and penalty weights have been chosen, unconstrained and constrained case are compared through nonlinear simulations. In the constrained case all the constraints given in equation (26) are active. We simulated the system during a sequence of steps in current demand. Figure 7 compares the trajectory of the compressor flow for the unconstrained and constrained case. Figure 8 shows the corresponding time history of the response. In both unconstrained and constrained simulations, during step changes in the demand, the ultracapacitor is used as a buffer. During step-up in demand, the current that is drawn from the fuel cell and passed through the

---

[4]A simple kinetic energy calculation shows that accelerating a 1000 kg vehicle from 20m/s to 21.5m/s (45 mph to 48 mph) in 1 second requires an almost 100 Amps increase in current on a 350 volt BUS.
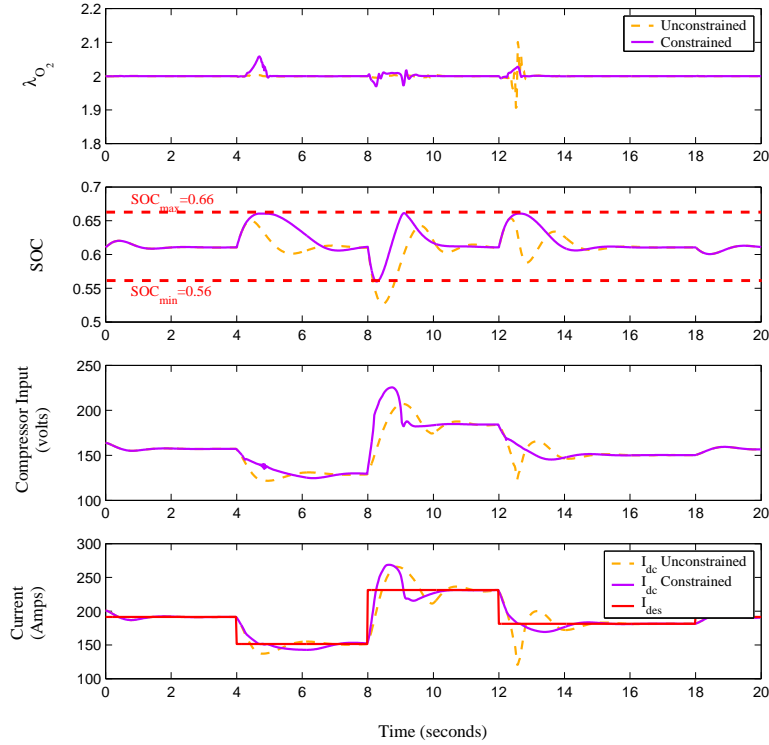
Figure 8: Influence on time response when surge constraint is enforced. The performance index weights are $Q = diag(0, 0, 100, 1)$, $S = diag(0.1, 0.001)$.

DC/DC convertor, I_{dc}, is initially less than the demand current, I_{des}, but rises smoothly to catch up with the demand. As a result oxygen deficit reduces to negligible levels as shown in both simulations. When the fuel cell current tops the demand, the ultracapacitor starts to recharge. Enforcing the constraints ensures that the state of charge remains between the specified bounds as shown in Fig. 8. At $t = 4$ a sudden 40 Amp dip in current results in compressor surge in the unconstrained system. In the constrained simulation, the current transient and consequently the compressor input transients are slowed down and as a result surge is prevented. At the same time the excess current charges the ultracapacitor as much as the ultracapacitor constraint allows. Once surge is inactive, the energy stored in the ultracapacitor is released and the state of charge is brought back to the desired level. A similar response can be seen at $t = 12$. Note that choke constraint is not activated even during the large step-up at $t = 8$.

Simulation also shows that beyond the surge line the compressor behavior is substantially different from prediction of the linearized model. This model mismatch causes the overall closed-loop response of the unconstrained system to degrade as can be seen at $t = 12$. Confining the compressor operation between the surge and choke lines, avoids regions with large model mismatch and results in improved closed-loop performance. Control of the hybrid fuel cell as explained above reduces the compressor overload that occurs during rapid load transients and might allow use of smaller compressors.

The simulations were performed on a 2 GHz Intel[5] Pentium processor on a Windows

This paragraph is a new addition which discusses the computation time required for solving the constrained versus the unconstrained problem.

16

XP [6] operating system. The unconstrained simulation did not require online optimization. Calculating the control gain and running the linear internal model required less than 0.3 seconds[7] for the 20 second unconstrained simulation shown in Fig. 8. This time does not include the runtime for the nonlinear plant since in reality the plant outputs are available through measurement and do not require simulation. The constrained simulation required solving a quadratic program online. For the 20-second simulation shown in Fig. 8, the total CPU time spent on optimization and running the linear internal model (and not including the simulation of the plant) was 20.1 seconds. The CPU time of 20.1 seconds for a 20-second constrained simulation is promising, even though we know that the state-of-the-art 2.0 GHz processor is considerably faster than the automotive microcontroller used in practice. It is also expected that the simulations can be executed more efficiently in a real-time environment. The feasibility of real-time implementation of a similar optimization-based control method for the same fuel cell system is shown in [36].

6   Conclusions

An ultracapacitor was utilized to prevent fuel cell oxygen starvation and air compressor surge during rapid load demands. A model predictive controller was designed for optimal distribution of current demand between the two power sources. Choice of model predictive control over conventional control methodologies was motivated by the need for smooth current split between the power sources and existence of hard constraints in the auxiliary power source and the air compressor. The controller performance was verified on a detailed nonlinear model of the fuel cell system. The controller performs well in splitting the demand between the fuel cell and the ultracapacitor. As a result, during a 100 Amp step-up in current in the hybrid architecture, the oxygen excess ratio always stays above 1.98, whereas in the stand alone fuel cell, oxygen excess ratio reaches the critical value of 1 as shown in [18]. Model predictive control enforces ultracapacitor constraints on state of charge and also prevents compressor surge.

7   Appendix

This Appendix provides a summary of fuel cell model governing equations and parameters. Table 1 lists the parameters and variables of the model. The model is explained in more detail in [19]. Tables 2 and 3 summarize the fuel cell and compressor equations, respectively.

---

[5]Intel is a registered trademark of Intel Corporation, Santa Clara, CA.

[6]Windows is a registered trademark of Microsoft Corporation, Seattle, WA.

[7]The cputime command in Matlab was used to get an estimate of the computation time.

Table 1: Model Variables and Parameters

A_{fc}	active area of the fuel cell
C_D	nozzle discharge coefficient
D_w	diffusion coefficient
F	Farady number
I	current
J	compressor inertia
M	molar mass
P	power
R	universal gas constant
T	temperature
V	volume
W	mass flow rate
d_c	compressor diameter
i	fuel cell current density (I/A_{fc})
m	mass
n	number of cells
n_d	electro-osmotic coefficient
p	pressure
t_m	membrane thickness
v	voltage
Ω	humidity ratio
γ	ratio of gas heat capacity
ϕ	relative humidity
ω	rotational speed
ρ_a	air density

Sub/Super scripts	
H_2	Hydrogen
N_2	Nitrogen
O_2	Oxygen
v	vapor
w	water
in	incoming
out	outgoing
rct	reacted
mbr	exchanged through membrane
$purge$	purged
an	anode
ca	cathode
cm	compressor motor
cp	compressor
fc	fuel cell
rm	return manifold
sm	supply manifold
st	stack

Table 2: The model governing equations

Physical Law Applied to	Equation
A1) Conservation of Mass: Cathode/Oxygen	$\frac{dm_{O_2}}{dt} = W_{O_2,in} - W_{O_2,out} - W_{O_2,rct}$
A2) Conservation of Mass: Cathode/Nitrogen	$\frac{dm_{N_2}}{dt} = W_{N_2,in} - W_{N_2,out}$
A3) Conservation of Mass: Cathode/Vapor	$\frac{dm_{w,ca}}{dt} = W_{v,ca,in} - W_{v,ca,out} + W_{v,gen} + W_{v,mbr}$
A4) Conservation of Mass: Supply Manifold	$\frac{dm_{sm}}{dt} = W_{cp} - W_{sm}$
A5) Conservation of Energy: Manifold Pressure	$\frac{dp_{sm}}{dt} = \gamma R \left(W_{cp}T_{cp} - W_{sm}T_{sm} \right) / (M_a^{atm} V_{sm})$
A6) Conservation of Energy: Air Compressor	$J_{cp}\frac{d\omega_{cp}}{dt} = \frac{1}{\omega_{cp}}\left(P_{cm} - P_{cp} \right)$
A7) Conservation of Energy (Isothermal): Return Manifold Pressure	$\frac{dp_{rm}}{dt} = RT_{st}\left(W_{ca} - W_{rm} \right) / (M_a^{ca} V_{rm})$
A8) Conservation of Mass: Hydrogen in the Anode	$\frac{dm_{H_2}}{dt} = W_{H_2,in} - W_{H_2,purge} - W_{H_2,rct}$
A9) Conservation of Mass: Vapor in the Anode	$\frac{dm_{w,an}}{dt} = W_{v,an,in} - W_{v,purge} - W_{v,mbr}$
A10) Psychrometric Law: Vapor Pressure	$p_{v,ca} = min\left[1, m_{w,ca}RT_{st}/(M_v V_{ca}p_{sat}^{st}) \right] p_{sat}^{st}$
A11) Dalton Law: Cathode Pressure	$p_{ca} = p_{O_2} + p_{N_2} + p_{v,ca}$
A12) Ideal Gas Law: Oxygen Pressure	$p_{O_2} = \frac{RT_{st}}{M_{O_2}V_{ca}}m_{O_2}$
A13) Ideal Gas Law: Nitrogen Pressures	$p_{N_2} = \frac{RT_{st}}{M_{N_2}V_{ca}}m_{N_2}$
A14) Ideal Gas Law: Manifold Air Temperature	$T_{sm} = \frac{p_{sm}V_{sm}M_a^{atm}}{Rm_{sm}}$
A15) Dalton/Ideal Gas Laws: Anode	$p_{an} = \frac{RT_{st}}{M_{H_2}V_{an}}m_{H_2} + min\left[1, \frac{RT_{st}m_{w,an}}{M_v V_{an}p_{sat}^{st}} \right] p_{sat}^{st}$
A16) Sub-Critical Nozzle Eq.(linearized) Supply Manifold Outlet	$W_{sm} = k_{sm}(p_{sm} - p_{ca})$
A17) Sub-Critical Nozzle Eq.: Return Manifold Flow	$W_{rm} = \frac{C_{D,rm}A_{T,rm}p_{rm}}{\sqrt{RT_{rm}}}\left(\frac{p_{atm}}{p_{rm}} \right)^{\frac{1}{\gamma}}\left\{ \frac{2\gamma}{\gamma-1}\left[1 - \left(\frac{p_{atm}}{p_{rm}} \right)^{\frac{\gamma-1}{\gamma}} \right] \right\}^{\frac{1}{2}}$
Critical Nozzle Eq.	$W_{rm} = \frac{C_{D,rm}A_{T,rm}p_{rm}}{\sqrt{RT_{rm}}}\gamma^{\frac{1}{2}}\left(\frac{2}{\gamma+1} \right)^{\frac{\gamma+1}{2(\gamma-1)}}$
A18) Partial Oxygen Flow	$W_{O_2,in} = 0.21\frac{M_{O_2}}{0.21M_{O_2}+0.79M_{N_2}}\frac{1}{1+\Omega_{atm}}W_{sm}$
A19) Partial Nitrogen Flow	$W_{N_2,in} = 0.79\frac{M_{N_2}}{0.21M_{O_2}+0.79M_{N_2}}\frac{1}{1+\Omega_{atm}}W_{sm}$
A20) Partial Vapor Flow	$W_{v,ca,in} = \frac{\Omega_{ca,in}}{1+\Omega_{atm}}W_{sm}$
A21) Atmospheric Humidity Ratio	$\Omega_{atm} = \frac{M_v}{M_a}\frac{\phi_{atm}p_{sat}^{atm}/p_{atm}}{1-\phi_{atm}p_{sat}^{atm}/p_{atm}}$
A22) Cathode Humidity Ratio	$\Omega_{ca,in} = \frac{M_v}{M_a}\frac{\phi_{ca,in}p_{sat}^{st}}{p_{sm}(1-\phi_{atm}p_{sat}^{atm}/p_{atm})}$
A23) Oxygen Outflow	$W_{O_2,out} = \frac{m_{O_2}}{m_{ca}}W_{ca}$
A24) Nitrogen Outflow	$W_{N_2,out} = \frac{m_{N_2}}{m_{ca}}W_{ca}$
A25) Vapor Outflow	$W_{v,ca,out} = \frac{p_{v,ca}V_{ca}M_v}{RT_{st}m_{ca}}W_{ca}$
A26) Reacted Oxygen	$W_{O_2,rct} = M_{O_2}\frac{nI_{st}}{4F}$
A27) Reacted Hydrogen	$W_{H_2,rct} = M_{H_2}\frac{nI_{st}}{2F}$
A28) Vapor Generated	$W_{v,gen} = M_v\frac{nI_{st}}{2F}$
A29) Mass Transport: Vapor diffusion	$W_{v,membr} = M_v A_{fc}n\left(n_d\frac{i}{F} - D_w\frac{\phi_{ca}-\phi_{an}}{t_m} \right)$
A30) Hydrogen flow	$W_{H_2,in} = \frac{1}{1+\Omega_{an,in}}W_{an,in}$
A31) Anode Vapor flow	$W_{v,an,in} = \frac{\Omega_{an,in}}{1+\Omega_{an,in}}W_{an,in}$
A32) Anode Humidity Ratio	$\Omega_{an,in} = \frac{M_v}{M_{H_2}}\frac{\phi_{an,in}p_{sat}^{an,in}}{p_{an,in}}$
A33) Dead-ended anode	$W_{v,purge} = 0$

Table 3: Calculation of Compressor Flow

Description	Equation
A34)Temperature Correction Factor	$\theta = T_{cp,in}/(288K)$
A35)Pressure Correction Factor	$\delta = p_{cp,in}/(1atm)$
A36)Compressor Speed Correction(rpm)	$N_{cr} = N_{cp}/\sqrt{\theta}$
A37)Air Mass Flow	$W_{cp} = W_{cr}\delta/\sqrt{\theta}$
A38)Corrected Air mass flow	$W_{cr} = \Phi\rho_a\frac{\pi}{4}d_c^2U_c$
A39)Compressor Blade Speed (m/s)	$U_c = \frac{\pi}{60}d_cN_{cr}$
A40)Normalized flow rate	$\Phi = \Phi_{max}\left[1 - exp\left(\beta(\frac{\Psi}{\Psi_{max}} - 1)\right)\right]$
A41)Dimensionless head parameter	$\Psi = \dfrac{C_pT_{cp,in}\left[\left(\frac{p_{cp,out}}{p_{cp,in}}\right)^{\frac{\gamma-1}{\gamma}} - 1\right]}{\frac{1}{2}U_c^2}$
A42)Polynomial functions	$\Phi_{max} = a_4M^4 + a_3M^3 + a_2M^2 + a_1M + a_0$
	$\beta = b_2M^2 + b_1M + b_0$
	$\Psi_{max} = c_5M^5 + c_4M^4 + c_3M^3 + c_2M^2 + c_1M + c_0$
A43)Inlet Mach Number	$M = \frac{U_c}{\sqrt{\gamma R_aT_{cp,in}}}$

8 Acknowledgements

References

[1] R.-H. Song, C.-S. Kim, and D.R. Shin, "Effects of flow rate and starvation of reactant gases on the performance of phosphoric acid fuel cells," *Journal of Power Sources*, vol. 86, pp. 289–293, 2000.

[2] G. Boehm, D. Wilkinson, S. Khight, R. Schamm, and N. Fletcher, "Method and apparatus for operating a fuel cell," *United States Patents 6,461,741*, 2002.

[3] J. Pukrushpan, A. Stefanopoulou, and H. Peng, "Control of fuel cell breathing," *IEEE Control Systems Magazine*, vol. 24, no. 2, pp. 30–46, April 2004.

[4] B. de Jager, "Rotating stall and surge control: a survey," *Proceedings of the 34th Conference on Decision and Control*, pp. 1857–1862, December 1995.

[5] P. Moraal and I. Kolmanovsky, "Turbocharger modeling for automotive control applications," *SAE Paper 1999-01-0908*, 1999.

[6] D. Boettner, G. Paganelli, Y. Guezennec, G. Rizzoni, and M. Moran, "Proton exchange membrane fuel cell system model for automotive vehicle simulation and control," *ASME Journal of Energy Resources Technology*, vol. 124, pp. 20–27, 2002.

[7] J. Sun and I. Kolmanovsky, "A robust load governor for fuel cell oxygen starvation protection," *Proceedings of the American Control Conference*, pp. 828–833, 2004.

[8] K. Rajashekara, "Propulsion system strategies for fuel cell vehicles," *SAE Paper 2000-01-0369*, 2000.

[9] N. Jalil, N.A. Kheir, and M. Salman, "A rule-based energy management strategy for a series hybrid vehicle," *Proceedings of American Control Conference*, pp. 689–693, 1997.

[10] Z. Fillipi, L. Louca, A. Stefanopoulou, J. Pukrushpan, B. Kittirungsi, and H. Peng, "Fuel cell APU for silent watch and mild electrification of a medium tactical truck," *SAE Paper No 2004-01-1477*, 2004.

[11] C.-C. Lin, H. Peng, J.-M. Kang, and J. Grizzle, "Power management strategy for a parallel hybrid electric truck," *IEEE Transactions on Control Systems Technology*, vol. 11, no. 6, pp. 839–849, 2003.

[12] A. Brahma, Y. Guezennec, and G. Rizzoni, "Optimal energy management in series hybrid electric vehicles," *Proceedings of the American Control Conference*, pp. 60–64, 2000.

[13] P. Rodatz, O. Garcia, L. Guzzella, F. Buchi, M. Bartschi, A. Tsukada, P. Dietrich, R. Kotz, G. Scherer, and A. Wokaun, "Performance and operational characteristics of a hybrid vehicle powered by fuel cells and supercapacitors," *SAE Paper 2003-01- 0418*, 2003.

[14] T. Matsumoto, N. Watanabe, H. Sugiura, and T. Ishikawa, "Development of fuel-cell hybrid vehicle," *SAE Paper No. 2002-01-0096*, 2002.

[15] L.P. Jarvis, P.J. Cygan, and M.P. Roberts, "Hybrid power source for manportable applications," *IEEE AESS Systems Magazine*, pp. 13–16, 2003.

[16] Y. Guezennec, T.-Y. Choi, G. Paganelli, and G. Rizzoni, "Supervisory control of fuel cell vehicles and its link to overall system efficiency and low-level control requirements," *Proceedings of the American Control Conference*, pp. 2055–2061, 2003.

[17] P. Rodatz, G. Paganelli, A. Sciarretta, and L. Guzzella, "Optimal power management of an experimental fuel cell supercapacitor-powered hybrid vehicle," *Control Engineering Practice*, vol. 13, pp. 41–53, 2005.

[18] A. Vahidi, A. Stefanopoulou, and H. Peng, "Model predictive control for starvation prevention in a hybrid fuel cell system," *Proceedings of American Control Conference*, pp. 834–839, 2004.

[19] J. Pukrushpan, A. Stefanopoulou, and H. Peng, *Control of Fuel Cell Power Systems: Principles, Modeling, Analysis, and Feedback Design*, Springer-Verlag, London, UK, 2004.

[20] J. Pukrushpan, H. Peng, and A. Stefanopoulou, "Control-oriented modeling and analysis for automotive fuel cell systems," *ASME Journal of Dynamic Systems, Measurement and Control*, vol. 126, pp. 14–25, 2004.

[21] P. Rodatz, G. Paganelli, and L. Guzzella, "Optimizing air supply control of a PEMFC fuel cell system," *Proceedings of the American Control Conference*, pp. 2043–2048, 2003.

[22] C.-C. Lin, H. Peng, J. Grizzle, and M.J. Kim, "Integrated dynamic simulation model with supervisory control strategy for a PEM fuel cell hybrid vehicle," *Proceedings of IMECE 2004 Proceedings of the ASME Dynamic Systems and Control Division*, vol. 73, pp. 275–286, 2004.

[23] J.M. Cunningham, M.A. Hoffman, R.M. Moore, and D.J. Friedman, "Requirements for flexible and realistic air supply model for incorporation into a fuel cell vehicle (FCV) system simulation," *SAE Paper 1999-01-2912*, 1999.

[24] M. Boyce, *Gas Turbine Engineering Handbook*, Gulf Publishing, Houston, Texas, 1982.

[25] J. Gravdahl and O. Egeland, *Compressor Surge and Rotating Stall*, Springer, London, UK, 1999.

[26] S. Piller, M. Perrin, and A. Jossen, "Methods for state-of-charge determination and their applications," *Journal of Power Sources*, vol. 96, pp. 113–120, 2001.

[27] J.M. Maciejowski, *Predictive Control with Constraints*, Prentice Hall, Essex, England, 2002.

[28] S. Qin and T. Badgwell, "A survey of industrial model predictive control technology," *Control Engineering Practice*, vol. 11, no. 7, pp. 733–764, July 2003.

[29] D. Mayne, J. Rawlings, C. Rao, and P. Scokaert, "Constrained model predictive control: Stability and optimality," *Automatica*, vol. 36, pp. 789–814, 2000.

[30] G. Pannocchia and J. Rawlings, "Disturbance models for offset-free model-predictive control," *AIChE Journal*, vol. 49, no. 2, pp. 426–437, 2003.

[31] K. Muske and T. Badgwell, "Disturbance modeling for offset-free linear model predictive control," *Journal of Process Control*, vol. 12, pp. 617–632, 2002.

[32] P. Tondel, T. Johansen, and A. Bemporad, "An algorithm for multi-parametric quadratic programming and explicit MPC solutions," *Automatica*, vol. 39, no. 3, pp. 489–497, March 2003.

[33] G. Franklin, D. Powell, and M. Workman, *Digital Control of Dynamic Systems*, Addison-Wesley, third edition, 1998.

[34] K.R. Muske and J.B. Rawlings, "Model predictive control with linear models," *AIChE Journal*, vol. 39, no. 2, pp. 262–287, 1993.

[35] D.W. Clarke, *Advances in Model-Based Predictive Control*, Oxford University Press, 1994.

[36] A. Vahidi, I.V. Kolmanovsky, and A. Stefanopoulou, "Constraint management in fuel cells: A fast reference governor approach," *Proceedings of American Control Conference*, pp. 834–839, 2005.